Acta Mech 232, 3591–3609 (2021)
https://doi.org/10.1007/s00707-021-03014-4

ORIGINAL PAPER

Xingquan Wang · Xia Liu · Qingsheng Yang

Transient analysis of diffusion-induced stress for hollow cylindrical electrode considering the end bending effect

Received: 18 January 2021 / Revised: 12 May 2021 / Accepted: 24 May 2021 / Published online: 29 June 2021

Abstract Lithiation and delithiation in electrodes lead to the evolution of internal stresses which may cause the mechanical degradation of batteries. In this work, the diffusion-induced stress of a hollow cylindrical electrode under either galvanostatic or potentiostatic charging is analytically solved based on a diffusion and mechanical coupled continuum model. The stress distributions at the end faces of the electrode with both ends traction free or fixed are also analyzed, the end effect of diffusion-induced bending is taken into account, and the resulting bending stresses are of practical importance for the stress distribution at the end faces. Using the obtained analytical expressions, a numerical example is given, and the results show that the stress distributions at the end faces change dramatically compared to the stresses remote from ends, both the charging mode and end constraints have significant effects on the distribution of stresses at the end faces of the electrodes, and the most dangerous location during the charging process is affected by the end's constraint conditions.

1 Introduction

Lithium-ion batteries are the dominant energy storage medium for portable electronic devices and electric vehicles due to their high energy density and long cyclic life. To improve the performance of lithium-ion batteries, thorough understanding of the failure mechanisms is of great necessity. Mechanical degradation is one of the primary modes of failure [1–3]. Lithiation and delithiation in electrodes during electrochemical charging and discharging result in volumetric strain in electrodes, lead to the evolution of internal stresses, and thereby induce damage and fracture of the active materials, causing the failure of batteries [4–7].

Mechanical degradation due to the insertion and extraction of Li ions in the electrodes is involved with the diffusion-induced stress (DIS) from the mechanics perspective. Prussin [8] analyzed the diffusion-induced stress in a thin plate based on the analogy between thermal stress and DIS. Subsequently, extensive works have addressed the evolution of diffusion-induced stress. Following the Fick's law, Lee et al. [9] studied the concentration distribution and diffusion-induced stress in a hollow cylinder with constant surface stress. The magnitude and distribution of diffusion-induced stresses were significantly affected by surface stress and surface energy, and the tensile stresses could decrease significantly due to the surface effects [10–12]. For potentiostatic or galvanostatic operation, the evolutions of diffusion-induced stress and strain energy were quite different [13], and the surface tangential stress in the discharge process for graphite evolved like decaying sinusoidal waves [14]. Deshpande et al. [15] showed that the concentration-dependent elastic modulus has a significant effect on the evolution of diffusion-induced stress in battery electrodes. Cai and Guo [16] not only considered the effect of concentration-dependent elastic modulus on diffusion-induced stresses in anisotropic anode particles, but also the effect of the concentration-dependent diffusion coefficient was studied. The core–shell structure model was usually applied to investigate the two-phase electrode particles, and discontinuities of diffusion-induced

X. Wang · X. Liu · Q. Yang (✉)
Department of Engineering Mechanics, Beijing University of Technology, Beijing 100124, China
e-mail: qsyang@bjut.edu.cn

stress were found because of the concentration jumps at the phase boundaries [17]. Zhang et al. [18] and Hu et al. [19] studied the effects of the composition gradient on the stress evolution in electrodes and demonstrated that the composition gradient could improve the mechanical performance of electrodes. In these works, the concentration gradient is always the driving force for the diffusion; however, it is also demonstrated that the diffusion-induced stress conversely influences the rate of lithium diffusion [20–23], and two-way coupling between stress and diffusion should be accounted. Christensen and Newman [20, 24] developed a mathematical model that coupled the hydrostatic pressure into the driving force for diffusion and reported that the maximum stress in lithium manganese oxide and graphite particles increased with particle size and charging rate. Cui et al. [25] proposed a stress-dependent chemical potential to investigate the insertion and extraction of lithium ions, and the effects of nonlinear, inelastic and finite deformation were accounted for. Anand [26] developed a unified framework which coupled the large elastic–plastic deformation with the Cahn–Hilliard-type species diffusion, and then, the effects of plasticity on the electrochemical performance of a-Si anodes were identified. Zhang et al. [27] developed a rate-dependent model to analyze the plastic flow and phase transformation in a cylindrical Si electrode, and the temporal evolution of the interface was captured by a diffusion model in the framework of Cahn–Hilliard phase-field theory. Chen et al. [28] investigated the cyclic plasticity behavior of an electrode subjected to a cyclic charging/discharging process, and the shakedown, ratcheting and fatigue responses were analyzed by both numerical method and experiments. Based on the free-energy imbalance inequality, Drozdov [29] derived a constitutive model for the viscoplastic response of the electrode to analyze the stresses in a spherical electrode particle. Bagheri et al. [30] proposed a constitutive theory for amorphous anode materials, and the viscoplastic deformations and microstructure evolution were accounted for. Introducing the mechanical potential [31] in the chemical potential, the continuum models that coupled diffusion and stress were presented [32–34], and the effect of hydrostatic stress on the diffusivity coefficient was also considered [35–37]. Recently, Chen and Huang [38] developed a self-consistent formulation that contains mechanical–diffusional–electrochemical coupling effects to study the variation of stress distribution and lithium-ion fraction of the electrodes.

To accommodate the mechanical degradation of electrodes caused by diffusion in the electrodes, various optimizing electrode structures have been used. For example, Holzapfel et al. [39] and Patel et al. [40] showed that the composite structures electrode can withstand the volume change to obtain better capacity retention and structure stability. Zhu et al. [41] evaluated the fatigue damage of a layered electrode plate under electrochemical cycling by the finite element method, and the results fitted well with experimental tests. Chan et al. [42] found that silicon nanowire electrodes can accommodate large strain upon lithiation and delithiation with little capacity fading. Xiao et al. [43] introduced a patterned structure on thin-film electrodes, the gaps between Si patterns provide stress relaxation, and the cycling stability of electrodes was improved. Bhandakkar and Gao [44] analyzed the diffusion-induced stress in a thin strip electrode, and the results suggested that nanoscale size can suppress crack formation under large diffusion-induced stresses. Yao et al. [45] compared the maximum tensile stresses of a sphere and a hollow sphere with an equal volume of Si, and the results indicated that the hollow structure reduced the maximum tensile stress. However, the geometry of the electrodes will affect the stress distribution and performance of the electrodes [36]. Zhang et al. [46] analyzed the diffusion-induced buckling of nanowires with radial diffusion or axial diffusion. The critical buckling time for the onset of buckling decreases with increasing wire length and current density, and the constraints to the ends of a wire play an important role in determining the critical buckling time [47–50]. Chakraborty et al. [51] found that the buckling also happened in cylinder electrodes for the diffusion-induced large compressive axial stress.

For hollow cylindrical electrodes, Guo et al. [52] considered the effects of hydrostatic stress and concentration-dependent elastic modulus on diffusion-induced stress (DIS) in a cylindrical Li-ion battery by finite element calculations using the commercial package COMSOL Multiphysics 3.5a. The distribution of diffusion-induced stress at the ends is more complicated because of local irregularities. Yang [53] considered the effect of diffusion-induced bending and obtained the analytical formulations of the diffusion-induced stresses of a hollow cylinder electrode under the potentiostatic operation, and the effect of stress on diffusion was not considered. To clarify the end effect caused by lithiation or delithiation, we adopted a continuum model of diffusion coupled with mechanics to analyze the stress evolutions of the electrode under either galvanostatic or potentiostatic condition, the effect of surface pressures and end bending was also considered, and the bending moment in Yang's work [53] has also been amended to be more reasonable. Analytical formulations of the diffusion-induced stresses at the end faces and remote from the ends were obtained. Numerical results showed that diffusion-induced bending had a significant effect on the stress distribution at end faces and both the charging mode and ends condition could affect the distribution of DIS in the electrodes.

2 Basic formulations for chemo-mechanical coupled model

Based on the theory of nonequilibrium thermodynamics, the diffusion equation with chemo-mechanical coupling term for homogenous isotropic media is given by [31, 54, 55]

$$\frac{\partial c}{\partial t} = Ag\nabla^2 c + A\widehat{b}\nabla^2, e \tag{1}$$

in which A is the species mobility and relates to the diffusion coefficient D as $A = \frac{Dc_0}{RT}$ (R is gas constant), g is the scalar chemistry modulus, e is the volume strain and $\widehat{b}$ is the chemistry-strain modulus expressed by the Lame constants λ and the G and chemical dilation coefficient β as follows:

$$\widehat{b} = -(2G + 3\lambda)\beta. \tag{2}$$

The diffusion equation is thermodynamically consistent and differs from Fick's second law for the mechanical effect on species diffusion is accounted. Its aimlessness in line with the diffusion equation given by Haftbaradaran et al. [56] where the hydrostatic pressure affects the diffusion is considered.

The field equation of motion with the inertia term and body force disregarded is given by

$$G\nabla^2\mathbf{u} + (\lambda + G)\nabla(\nabla \cdot \mathbf{u}) + \widehat{b}\nabla c = 0. \tag{3}$$

In the framework of linear elasticity, the isotropic constitutive relation between the stress and strain with the effect of diffusion is expressed as

$$\boldsymbol{\sigma} = 2G\boldsymbol{\varepsilon} + \left(\lambda e + \widehat{b}c\right)\mathbf{I}. \tag{4}$$

Consider a homogeneous isotropic hollow cylinder with inner radius a and outer radius b, as shown in Fig. 1. The cylindrical coordinate system (r, θ, z) is used where r is the radial direction, θ is the circumferential direction and z is the cylinder axis direction. For axisymmetric problem, the field variables are independent of θ, and the displacement components are $u_r = u_r(r, z, t)$, $u_\theta = 0$ and $u_z = u_z(r, z, t)$. The strain components can be calculated from the displacement as

$$\varepsilon_r = \frac{\partial u_r}{\partial r}, \quad \varepsilon_\theta = \frac{u_r}{r}, \quad \varepsilon_z = \frac{\partial u_z}{\partial z} \quad \text{and} \quad \gamma_{rz} = \frac{\partial u_r}{\partial z} + \frac{\partial u_z}{\partial r}. \tag{5}$$

Then, the Navier equation in the cylindrical coordinate system can be obtained as:

$$\widehat{b}\frac{\partial c}{\partial r} + (\lambda + 2G)\frac{\partial e}{\partial r} - G\left(-\frac{\partial^2 u_r}{\partial z^2} + \frac{\partial^2 u_z}{\partial r \partial z}\right) = 0, \tag{6}$$

$$\widehat{b}\frac{\partial c}{\partial z} + (\lambda + 2G)\frac{\partial e}{\partial z} - G\left(\frac{1}{r}\frac{\partial u_r}{\partial z} - \frac{1}{r}\frac{\partial u_z}{\partial r} + \frac{\partial^2 u_r}{\partial r \partial z} - \frac{\partial^2 u_z}{\partial r^2}\right) = 0, \tag{7}$$

and the volume strain is

$$e = \mathrm{div}\mathbf{u} = \frac{1}{r}\frac{\partial (r u_r)}{\partial r} + \frac{\partial u_z}{\partial z}. \tag{8}$$

The Laplace operator for the axisymmetric situation is

$$\nabla^2 = \frac{\partial^2}{\partial r^2} + \frac{1}{r}\frac{\partial}{\partial r} + \frac{\partial^2}{\partial z^2}. \tag{9}$$

It is easily seen from Eqs. (6) and (7) that the volume strain and the species concentration have the following important relation:

$$\nabla^2 e = -\frac{\widehat{b}}{\lambda + 2G}\nabla^2 c. \tag{10}$$

Substituting Eq. (10) in Eq. (1), the diffusion equation with chemo-mechanical coupling term is

$$\frac{\partial c}{\partial t} = A\left(g - \frac{\widehat{b}^2}{\lambda + 2G}\right)\nabla^2 c. \tag{11}$$

The second term in the right-hand side of Eq. (11) represents the coupling effect on the diffusion, and it shows that the volume strain varies with the change in concentration and affects the diffusion processes conversely.

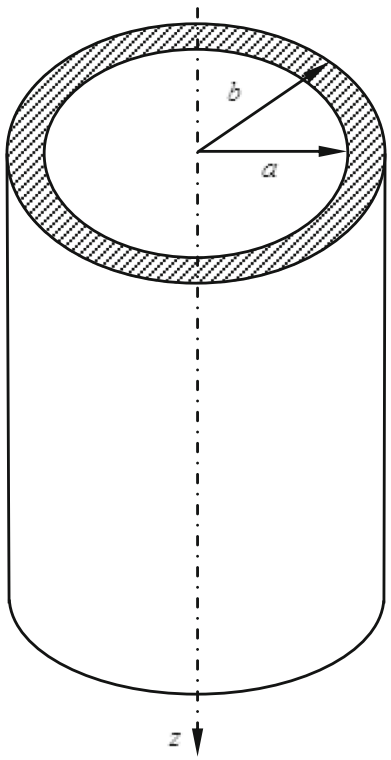

Fig. 1 The sketch of hollow cylindrical electrode

3 Analytical solutions for a hollow cylindrical electrode

Assuming that the length of the hollow cylinder is long enough or finite with both ends completely constrained, then the axial displacement component can be ignored, and the nonzero displacement in the electrode is $u = u_r(r, t)$ and strain–displacement relations are

$$\varepsilon_{rr} = \frac{\mathrm{d}u_r}{\mathrm{d}r}, \quad \varepsilon_{\theta\theta} = \frac{u_r}{r}. \tag{12}$$

The equation of motion is simplified as

$$\frac{\partial^2 u_r}{\partial r^2} + \frac{1}{r}\frac{\partial u_r}{\partial r} - \frac{u_r}{r^2} = -\frac{\widehat{b}}{\lambda + 2G}\frac{\partial c}{\partial r}. \tag{13}$$

The radial displacement can be found by integration as

$$u = \frac{(1+v)\beta}{1-v}\frac{1}{r}\int_a^r cr\mathrm{d}r + C_1 r + \frac{C_2}{r}, \tag{14}$$

where v is the Poisson's ratio and C_1 and C_2 are the constants to be determined from boundary conditions. The stresses components can be deduced by using Eq. (14) in Eq. (4),

$$\sigma_{rr} = -\frac{\beta E}{1-v}\frac{1}{r^2}\int_a^r cr\mathrm{d}r + \frac{C_1 E}{(1+v)(1-2v)} - \frac{C_2 E}{(1+v)r^2}, \tag{15}$$

$$\sigma_{\theta\theta} = -\frac{\beta E}{1-v}c + \frac{\beta E}{1-v}\frac{1}{r^2}\int_a^r cr\mathrm{d}r + \frac{C_1 E}{(1+v)(1-2v)} + \frac{C_2 E}{(1+v)r^2}, \tag{16}$$

$$\sigma_{zz} = \frac{2C_1 E v}{(1+v)(1-2v)} - \frac{\beta E}{1-v}c, \tag{17}$$

where E represents the modulus of elasticity.

The hollow cylinder is supposed to be subject to inner pressure P_0 and external pressure P_1, that is,

$$\sigma_{rr} = P_0 \quad \text{at} \quad r = a, \tag{18}$$

$$\sigma_{rr} = P_1 \quad \text{at} \quad r = b. \tag{19}$$

The constants C_1 and C_2 can be obtained from the boundary conditions (18) and (19):

$$C_1 = \frac{(1+v)(1-2v)}{E}\left[\frac{b^2P_1 - a^2P_0}{b^2-a^2} + \frac{E\beta}{1-v}\frac{1}{b^2-a^2}\int_a^b cr\mathrm{d}r\right], \tag{20}$$

$$C_2 = \frac{1+v}{E}\left[\frac{b^2a^2(P_1-P_0)}{b^2-a^2} + \frac{E\beta}{1-v}\frac{a^2}{b^2-a^2}\int_a^b cr\mathrm{d}r\right]. \tag{21}$$

Then, the displacement and stresses in Eqs. (14)–(17) can be expressed as

$$\begin{aligned} u = {} & \frac{1+v}{E}\left[\frac{1}{r}\frac{b^2a^2(P_1-P_0)}{b^2-a^2} + (1-2v)r\frac{b^2P_1-a^2P_0}{b^2-a^2}\right] \\ & + \frac{(1+v)\beta}{1-v}\left[\frac{1}{r}\int_a^r cr\mathrm{d}r + \frac{1}{r}\frac{a^2}{b^2-a^2}\int_a^b cr\mathrm{d}r + (1-2v)\frac{r}{b^2-a^2}\int_a^b cr\mathrm{d}r\right], \end{aligned} \tag{22}$$

$$\sigma_{rr} = \frac{b^2P_1}{b^2-a^2}\left(1-\frac{a^2}{r^2}\right) - \frac{a^2P_0}{b^2-a^2}\left(1-\frac{b^2}{r^2}\right) + \frac{\beta E}{1-v}\frac{1}{r^2}\left[-\int_a^r cr\mathrm{d}r + \frac{r^2-a^2}{b^2-a^2}\int_a^b cr\mathrm{d}r\right], \tag{23}$$

$$\sigma_{\theta\theta} = \frac{b^2P_1}{b^2-a^2}\left(1+\frac{a^2}{r^2}\right) - \frac{a^2P_0}{b^2-a^2}\left(1+\frac{b^2}{r^2}\right) - \frac{\beta E}{1-v}c + \frac{\beta E}{1-v}\frac{1}{r^2}\left[\int_a^r cr\mathrm{d}r + \frac{r^2+a^2}{b^2-a^2}\int_a^b cr\mathrm{d}r\right], \tag{24}$$

$$\sigma_{zz} = \frac{2v\left(b^2P_1 - a^2P_0\right)}{b^2-a^2} + \frac{2v\beta E}{1-v}\frac{1}{b^2-a^2}\int_a^b cr\mathrm{d}r - \frac{\beta E}{1-v}c. \tag{25}$$

These are the displacement and stress distribution in the hollow cylinder far away from the cylinder end when the strain in the direction of the z-axis is zero. They can deteriorate into the elastic solutions of an infinite cylinder subjected to internal and external pressure with the chemical terms neglected.

For a finite length cylinder with both ends free, there will be boundary conditions $\sigma_{zz} = 0$ at both ends. Assuming that the other initial and boundary conditions for concentration and stresses should be maintained, then it is impossible to satisfy $\sigma_{zz} = 0$ at each point. Therefore, we make the resultant forces at both ends zero to satisfy the boundary conditions approximately,

$$\int_a^b \sigma_{zz} \cdot 2\pi r\mathrm{d}r = 0. \tag{26}$$

Adding a constant Q to the stress σ_{zz} shown in Eq. (25) makes Eq. (26) come true, that is,

$$\int_a^b \left\{\left[\frac{2v\left(b^2P_1 - a^2P_0\right)}{b^2-a^2} + \frac{2v\beta E}{1-v}\frac{1}{b^2-a^2}\int_a^b cr\mathrm{d}r - \frac{\beta E}{1-v}c\right] + Q\right\} \cdot 2\pi r\mathrm{d}r = 0. \tag{27}$$

After integration, Q can be solved as

$$Q = -\frac{2v\left(b^2P_1 - a^2P_0\right)}{b^2-a^2} + \frac{2\beta E}{b^2-a^2}\int_a^b cr\mathrm{d}r. \tag{28}$$

Superpositioning Eqs. (28) and (25), the axial stress expression far away from the ends for a finite length hollow cylinder with both ends free is obtained to

$$\sigma_{zz} = \frac{E\beta}{1-v}\left[\frac{2}{b^2-a^2}\int_a^b cr\mathrm{d}r - c\right]. \tag{29}$$

At both ends of the hollow cylinder, the axial stress is still not equal to zero, but its resulting force is equal to zero. The stresses σ_{rr} and $\sigma_{\theta\theta}$ far away from the ends remain the same as shown in Eqs. (23) and (24), and the displacement is changed as to

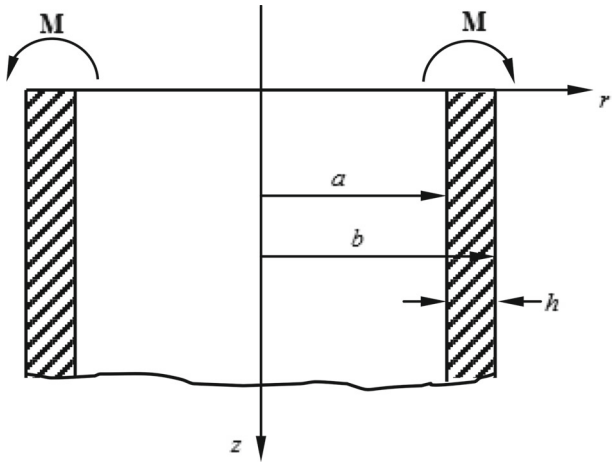

Fig. 2 The bending moments at end faces for traction free ends condition

$$u = \frac{1+v}{E}\left[\frac{1}{r}\frac{b^2a^2(P_1-P_0)}{b^2-a^2} + \frac{1-v}{1+v}r\frac{b^2P_1-a^2P_0}{b^2-a^2}\right] + \frac{(1+v)\beta}{1-v}\left[\frac{1}{r}\int_a^r cr\mathrm{d}r + \frac{1}{r}\frac{a^2}{b^2-a^2}\int_a^b cr\mathrm{d}r + \frac{1-3v}{1+v}\frac{r}{b^2-a^2}\int_a^b cr\mathrm{d}r\right]. \tag{30}$$

In the foregoing discussion, we considered the stresses far away from the ends; however, the stress distribution is more complicated near the ends due to local irregularities. For the hollow cylinder with both ends free, Eq. (29) requires that the normal stress caused by nonuniform distribution of concentration in the radial direction should be distributed over the ends of the cylinder. To have a free end, the stress produced by forces equal and opposite to that shown in Eq. (29) must be superposed. Those forces can be reduced to bending moments **M** at the end faces, shown in Fig. 2, and introduce the deflection of the hollow cylinder near the ends. Supposing the hollow cylinder is long enough that the free end condition will have an impact only locally, then take any end of the cylinder as a representative for analysis. The bending moments are uniformly distributed at the end faces as

$$M = -\int_a^b \sigma_{zz}\left(r-\frac{a+b}{2}\right)\cdot 1\mathrm{d}r = -\int_a^b \frac{E\beta}{1-v}\left[\frac{2}{b^2-a^2}\int_a^b cr\mathrm{d}r - c\right]\left(r-\frac{a+b}{2}\right)\cdot 1\mathrm{d}r = -\frac{E\beta}{1-v}\left(\frac{a+b}{2}\int_a^b c\mathrm{d}r - \int_a^b cr\mathrm{d}r\right). \tag{31}$$

Evidently, the maximum deflection is at the ends, and the resultant hoop stress at the end faces of a thin-walled cylinder of thickness h with traction free conditions is [57]

$$\sigma_{\theta\theta}^{E} = \frac{b^2P_1}{b^2-a^2}\left(1+\frac{a^2}{r^2}\right) - \frac{a^2P_0}{b^2-a^2}\left(1+\frac{b^2}{r^2}\right) + \frac{E\beta}{1-v}\frac{1}{r^2}\left(\frac{r^2+a^2}{b^2-a^2}\int_a^b cr\mathrm{d}r + \int_a^r cr\mathrm{d}r - cr^2\right) + \frac{E\beta}{2(1-v)\chi^2K}\frac{E}{r}\times\left(\int_a^b cr\mathrm{d}r - \frac{a+b}{2}\int_a^b c\mathrm{d}r\right) - \frac{E\beta v}{1-v}\left(\frac{2}{b^2-a^2}\int_a^b cr\mathrm{d}r - c\right), \tag{32}$$

where $\chi = \sqrt[4]{\frac{3(1-v^2)}{\left(\frac{a+b}{2}\right)^2h^2}}$[4] $\frac{3(1-v^2)}{\left(\frac{a+b}{2}\right)^2h^2}$ and $K = \frac{Eh^3}{12(1-v^2)}$ is the flexural rigidity of the strip on the hollow cylinder in the axial direction. The axial stress at the end face is ignored because the resultant force in axial direction is zero under free ends condition.

For the hollow cylinder of length l with both ends completely constrained, the built-in condition was adopted at each end to approximate the mechanical constraint. In addition to the case of a hollow cylinder with both ends free, any end of the cylinder can be taken as representative for the analysis, supposing that the

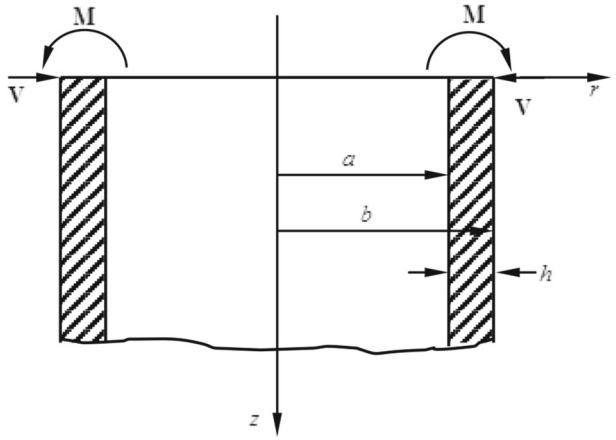

Fig. 3 The shear force and bending moments at end faces for fixed end condition

hollow cylinder is long enough. The built-in condition introduces shear forces **V** and bending moments **M** on the end surfaces of the hollow cylinder, shown in Fig. 3, and the deflection caused by these reaction forces **V** and moments **M** can be found as [57]

$$w = \frac{e^{-\chi z}}{2\chi^3 K}[V\cos\chi z - M\chi(\cos\chi z - \sin\chi z)], \tag{33}$$

where the shear force **V** and bending moments **M** per unit length of the edge can be found by the built-in conditions

$$M = -\frac{2\chi^2 K(1+v)}{E}\left[\frac{1}{b}\frac{b^2a^2(P_1-P_0)}{b^2-a^2} + (1-2v)b\frac{b^2P_1-a^2P_0}{b^2-a^2}\right] - 4\chi^2 K\beta(1+v)\frac{b}{b^2-a^2}\int_a^b cr\mathrm{d}r, \tag{34}$$

$$V = -\frac{4\chi^3 K(1+v)}{E}\left[\frac{1}{b}\frac{b^2a^2(P_1-P_0)}{b^2-a^2} + (1-2v)b\frac{b^2P_1-a^2P_0}{b^2-a^2}\right] - 8\chi^3 K\beta(1+v)\frac{b}{b^2-a^2}\int_a^b cr\mathrm{d}r. \tag{35}$$

Notice that the largest deflection caused by these reaction forces at the end face occurs at $z = 0$ and the corresponding average hoop stress and axial stress are

$$\sigma_{\theta\theta}^b = -\frac{(1+v)}{a}\left[\frac{1}{b}\frac{b^2a^2(P_1-P_0)}{b^2-a^2} + (1-2v)b\frac{b^2P_1-a^2P_0}{b^2-a^2}\right] - 2\beta(1+v)\frac{E}{a}\frac{b}{b^2-a^2}\int_a^b cr\mathrm{d}r \tag{36}$$

$$\sigma_{zz}^b = \frac{24\chi^2 K(1+v)}{Eh^3}\left(r-\frac{a+b}{2}\right)\left[\frac{1}{b}\frac{b^2a^2(P_1-P_0)}{b^2-a^2} + (1-2v)b\frac{b^2P_1-a^2P_0}{b^2-a^2}\right] + \frac{48\chi^2 K\beta(1+v)}{h^3}\left(r-\frac{a+b}{2}\right)\frac{b}{b^2-a^2}\int_a^b cr\mathrm{d}r. \tag{37}$$

Thus, the resultant hoop stress near the end faces of the thick wall hollow cylinder with both ends constrained can be approximated as

$$\begin{aligned}\sigma_{\theta\theta}^E = {} & \frac{b^2P_1}{b^2-a^2}\left(1+\frac{a^2}{r^2}\right) - \frac{a^2P_0}{b^2-a^2}\left(1+\frac{b^2}{r^2}\right) + \frac{\beta E}{1-v}\frac{1}{r^2}\left[\frac{r^2+a^2}{b^2-a^2}\int_a^b cr\mathrm{d}r + \int_a^r cr\mathrm{d}r - cr^2\right] \\ & - \left(\frac{(1+v)}{a} - \frac{24v\chi^2K(1+v)}{Eh^3}\left(r-\frac{a+b}{2}\right)\right)\left[\frac{1}{b}\frac{b^2a^2(P_1-P_0)}{b^2-a^2} + (1-2v)b\frac{b^2P_1-a^2P_0}{b^2-a^2}\right] \\ & - 2\beta(1+v)\frac{b}{b^2-a^2}\left(\frac{E}{a} - \frac{24v\chi^2K}{h^3}\left(r-\frac{a+b}{2}\right)\right)\int_a^b cr\mathrm{d}r\end{aligned} \tag{38}$$

and the resultant axial stress is

$$\sigma_{zz}^{E} = \frac{2v\left(b^2P_1 - a^2P_0\right)}{b^2 - a^2} + \frac{\beta E}{1-v}\left(\frac{2v}{b^2-a^2}\int_a^b cr\mathrm{d}r - c\right) + \frac{24\chi^2K(1+v)}{Eh^3}\left(r - \frac{a+b}{2}\right)\left[\frac{1}{b}\frac{b^2a^2(P_1-P_0)}{b^2-a^2} + (1-2v)b\frac{b^2P_1 - a^2P_0}{b^2-a^2}\right] + \frac{48\chi^2K\beta(1+v)}{h^3}\left(r - \frac{a+b}{2}\right)\frac{b}{b^2-a^2}\int_a^b cr\mathrm{d}r. \tag{39}$$

It should be noted that the length of the hollow cylinder in the preceding discussion is assumed to be large. If this is not the case, the bending at one end cannot be considered as independent of the conditions at the other end, and a more detailed discussion of the stress distribution becomes necessary.

Considering the diffusion of lithium into a hollow cylinder electrode, the transport of lithium ions in this axisymmetric case can be obtained from Eq. (11) as

$$\frac{\partial c}{\partial t} = Am\left(\frac{\partial^2 c}{\partial r^2} + \frac{1}{r}\frac{\partial c}{\partial r}\right), \tag{40}$$

where $m = g - \frac{\widehat{b}^2}{\lambda+2G}$. Suppose that the initial Li-ion concentration in the hollow cylinder is zero, that is,

$$c(r,0) = 0. \tag{41}$$

For a galvanostatic charging process, the Neumann boundary condition is applied:

$$Am\left.\frac{\partial c(r,t)}{\partial r}\right|_{r=a} = 0 \quad \text{for} \quad t \geq 0, \tag{42}$$

$$Am\left.\frac{\partial c(r,t)}{\partial r}\right|_{r=b} = \frac{i_n}{F} \quad \text{for} \quad t \geq 0, \tag{43}$$

where $F = 96{,}485.3\ \mathrm{Cmol}^{-1}$ is the Faraday's constant and i_n is the applied current density flowing into the electrode. But, to simulate the potentiostatic charging, the boundary conditions are

$$\left.\frac{\partial c(r,t)}{\partial r}\right|_{r=a} = 0 \quad \text{for} \quad t \geq 0, \tag{44}$$

$$c(r,t)|_{r=b} = c_0 \quad \text{for} \quad t \geq 0, \tag{45}$$

where c_0 is the constant surface concentration.

Using the method of separation of variables, the solutions of Eq. (40) with initial boundary conditions for galvanostatic and potentiostatic charging can be solved analytically [58, 59], and the concentration expression for galvanostatic charging is

$$c = \frac{i_n b}{FAm}\left\{\frac{2Amt}{b^2-a^2} + \frac{r^2}{2\left(b^2-a^2\right)} - \frac{a^2\ln r}{b^2-a^2} - \frac{b^3-a^3}{6(b-a)\left(b^2-a^2\right)} + \frac{a^2\left(b\ln b - b - a\ln a + a\right)}{(b-a)\left(b^2-a^2\right)} + \sum_{n=1}^{\infty} A_n\left[\mathrm{Y}_1(\xi_n a)\,\mathrm{J}_0(\xi_n r) - \mathrm{J}_1(\xi_n a)\,\mathrm{Y}_0(\xi_n r)\right]\mathrm{e}^{-Am\xi_n^2 t}\right\}, \tag{46}$$

where J_i and Y_i are the Bessel functions of order i of the first and second kind, respectively. ξ_n must be the positive roots of the equation

$$\mathrm{J}_1(\xi a)\mathrm{Y}_1(\xi b) - \mathrm{Y}_1(\xi a)\mathrm{J}_1(\xi b) = 0. \tag{47}$$

The coefficients A_n are given by

$$A_n = -\frac{\pi^2}{2}\frac{\mathrm{J}_1^2(\xi_n b)}{\mathrm{J}_1^2(\xi_n b) - \mathrm{J}_1^2(\xi_n a)}[\mathrm{J}_1(\xi_n a)\mathrm{Y}_0(\xi_n b) - \mathrm{Y}_1(\xi_n a)\mathrm{J}_0(\xi_n b)]. \tag{48}$$

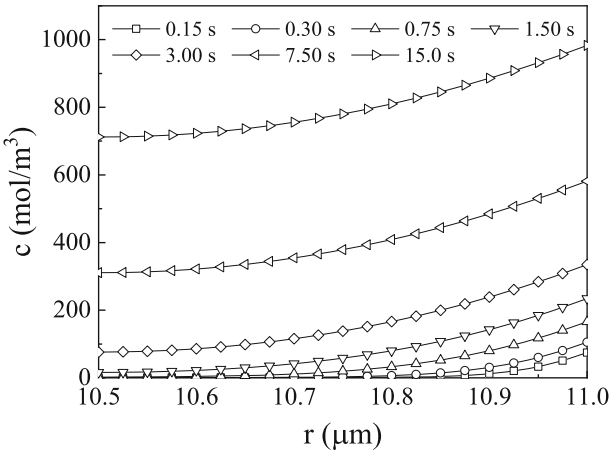

Fig. 4 The distribution of concentration at different times under galvanostatic charging

But for potentiostatic charging, the concentration expression is provided as [58, 59]

$$c = c_0\left\{1 - \pi\sum_{n=1}^{\infty}\frac{\mathrm{J}_0(b\zeta_n)\mathrm{J}_1(a\zeta_n)}{\mathrm{J}_0^2(b\zeta_n) - \mathrm{J}_1^2(a\zeta_n)}[\mathrm{J}_1(a\zeta_n)\mathrm{Y}_0(r\zeta_n) - \mathrm{J}_0(r\zeta_n)\mathrm{Y}_1(a\zeta_n)]e^{-Am\zeta_n^2 t}\right\}, \tag{49}$$

where ζ_n are the positive roots of the following equation:

$$\mathrm{J}_0(b\zeta_n)\mathrm{Y}_1(a\zeta_n) - \mathrm{J}_1(a\zeta_n)\mathrm{Y}_0(b\zeta_n) = 0. \tag{50}$$

Applying the concentration expressions in the equations for stresses, the diffusion-induced stresses both at or away from the end faces of the hollow cylinder can be obtained.

4 Results and discussion

Using the above solutions, we consider a thin-walled hollow cylindrical electrode of inner radius 10.5 μm and outer radius 11.0 μm. For simplicity, the uniform pressure on the inner and outer surfaces of the electrode is supposed to be zero. The material parameters used here are $D = 1.76 \times 10^{-15}$ m^2/s, $\upsilon = 0.2$, $\beta = 1.92 \times 10^{-6}$ m^3/mol $E = 70$ GPa and $c_0 = 2.3 \times 10^4$ mol/m^3 [60]. The chemistry modulus g is estimated from the relationship between chemical potential and concentration as $g = 1.56$ J $\cdot$ m^3/mol^2.

4.1 The stress distribution under galvanostatic charging

The concentration distribution for galvanostatic charging at different times is shown in Fig. 4, and it is evident that the Li concentration in the electrode increases gradually with time and that it decreases from the outer surface to inner surface at any time, since there is a constant surface flux at the outer surface. The distribution curves of Li concentration along the radius are almost parallel to each other after 7.50 s (about $\frac{0.5(b-a)^2}{Am}$), which indicates that the Li concentration on the whole hollow cylindrical electrode nearly keeps a stable and uniform growth after 7.50 s.

Figure 5 shows the variations of the stress components away from the ends at different times, and the radial stress and hoop stress are the same under free ends condition or fixed ends condition and are shown in Figs. 5a, b, respectively. From Fig. 5a, we note that the radial stress is tensile at all points and becomes zero at the inner and outer surface of the hollow cylinder. The value of the tensile stress gradually increases with time until 7.50 s, and after that, it remains stable. However, Fig. 5b shows that the hoop stress is tensile at the inner surface and compressive at the outer surface, it has its largest numerical value at the inner and outer surfaces of the electrode, and its value also increases until 7.50 s. It is known that the diffusion of Li concentration causes the expansion of the hollow cylindrical electrode, and for the galvanostatic charging considered here, the concentration at outer surface is larger than at the inner surface, which leads to circumferential compressive

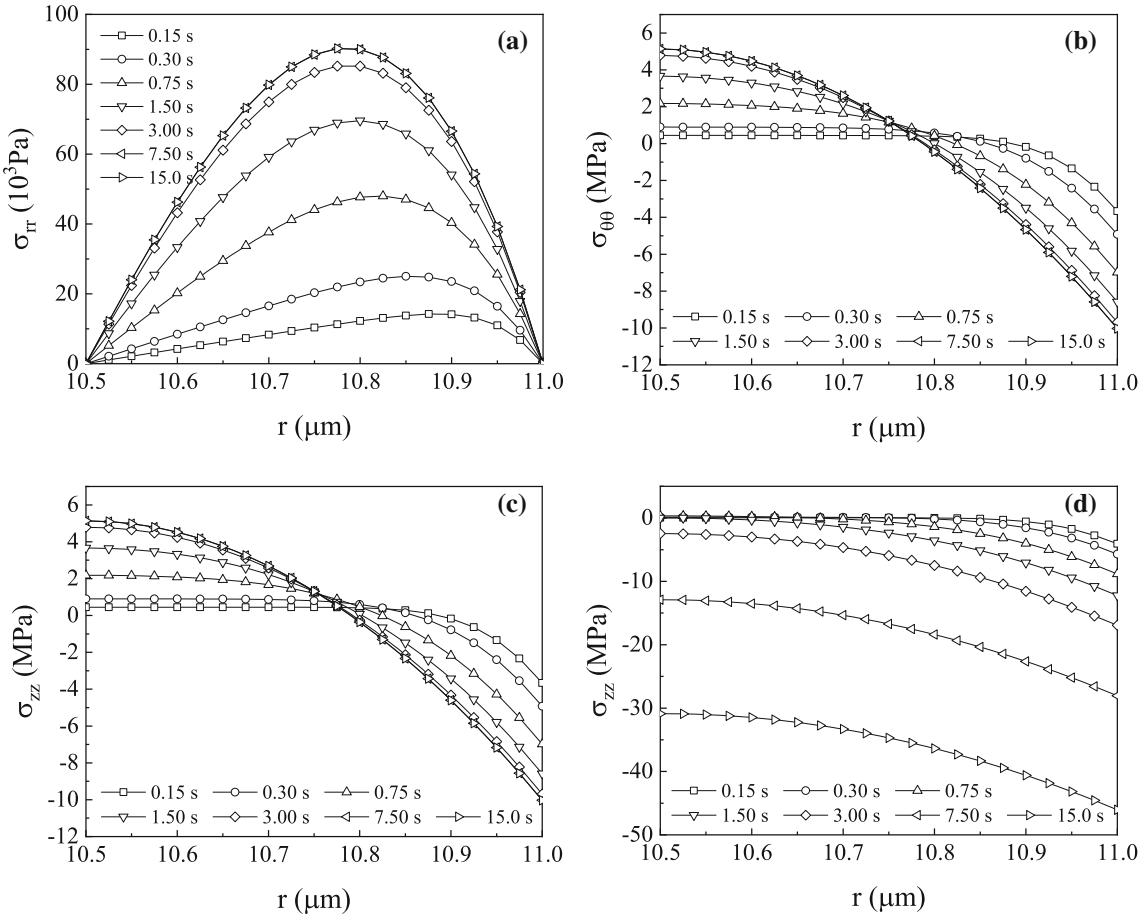

Fig. 5 Stress distributions away from the ends at different times under galvanostatic charging: **a** radial stress, **b** hoop stress, **c** axial stress under traction free ends condition, **d** axial stress under fixed ends condition

stress at the outer surface but circumferential tensile stress at the inner surface and radial tensile stress at all points. The increases of the stress values are due to the raise of the Li concentration in the electrode, and the stable and uniform growth of concentration after 7.50 s results in the stable stress state at last.

Figure 5c shows the axial stress of points remote from the ends under free ends condition, and it is also tensile at the inner surface and compressive at the outer surface. That is because the axial expansion at the outer surface caused by diffusion is constrained by the surrounding materials and leads to a stretch of the inner surface. We also note that at the inner and outer surfaces, the value of axial stress is the same as that of hoop stress under free ends condition, and it is because Eq. (24) is equal to Eq. (29) at the surfaces.

Figure 5d shows the variation of the axial stress away from the ends under fixed ends condition, and it shows that the hollow cylindrical electrode gets into a state of compression in the axial direction, and the compressive stress increases with the rise of concentration constantly; since both ends of the electrode are constrained, the diffusion-induced expansion is restricted in the axial direction.

For the thin hollow cylindrical electrode with the traction free end faces, the resultant axial stress at the end faces is zero, and the variation of the resultant hoop stress at the end faces for different times is shown in Fig. 6. It is evident that the hoop stress at the end faces is different from that away from the ends because of the local bending effect caused by diffusion. In Fig. 7, the hoop stress at the end faces and that away from the ends are compared, and it shows that the tensile stress at the inner face is enlarged and the compressive stress at the outer surface is reduced, since the local bending causes stretch in circumferential direction. This bending-induced hoop stress at the end faces is always at the tensile state, and it also increases similar to the axial stress remote from the ends. The maximum tensile stress at the free end of the thin-walled electrode is 74% greater than the stress at points remote from the ends under galvanostatic operation.

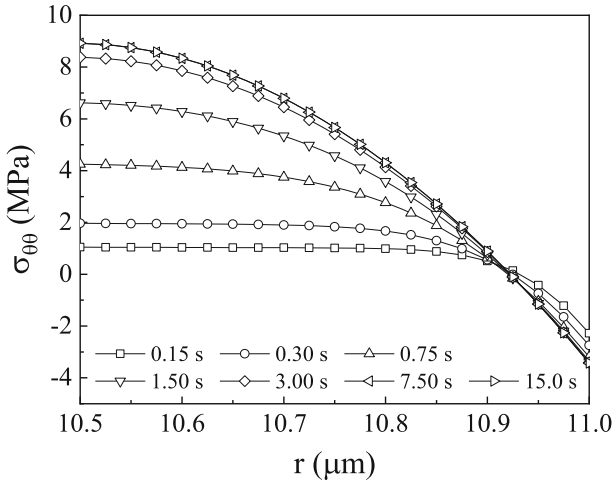

Fig. 6 Hoop stress distributions at the end faces for different times under galvanostatic charging and traction free ends condition

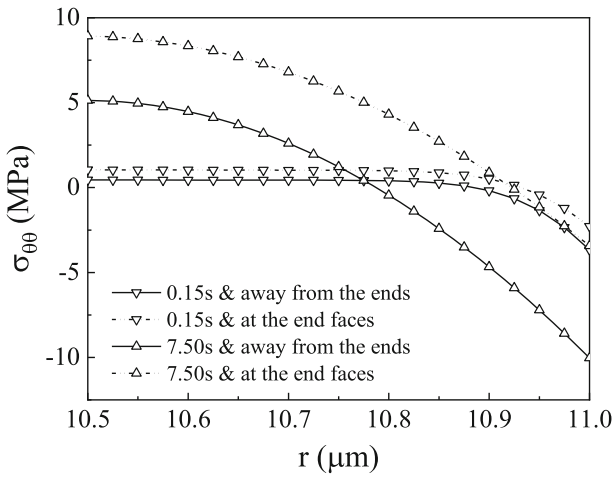

Fig. 7 The comparison of hoop stress at end faces and away from ends under galvanostatic charging and traction free ends condition

In order to predict the most dangerous location during the charging process, the von Mises equivalent stress in the cylindrical electrode is analyzed. Figure 8 shows the comparison of equivalent stress at the end faces and away from the ends under galvanostatic charging and traction free ends condition. The von Mises equivalent stress both at the end faces and away from the ends increases during the charging process, and the increment of the equivalent stresses gradually slowing down for the distribution of stress components in electrode tends to be stable. Though the end bending affects the distribution of stresses at the end face, the maximum equivalent stress for the hollow cylindrical electrode under galvanostatic charging and traction free ends condition still occurs at the outer surface away from the ends.

For the case of both ends fixed, the distribution of the resultant hoop stress and axial stress at the end faces for different times is shown in Figs. 9 and 10, respectively. Figure 9 shows that the hoop stress gets compressive at the whole end faces, and its value also increases continuously with rising Li concentration. This is because the fixed ends prevent the ascent of the circumference of the end faces of the thin-wall electrode caused by chemical expansion, thus imposing a great constraint on the end faces in the circumferential direction. This constraint will increase with the concentration and leads to an increase of compressive stress at the end faces. The maximum compressive stress occurs on the edge of the end faces, and it transfers from the outer edge to the inner edge with the ongoing galvanostatic operation.

From Fig. 10, we note that the axial stress at the end faces is compressive on the inner edge, while it is first compressive and then tensile on the outer edge. Compared to Fig. 5d which shows the axial stress remote

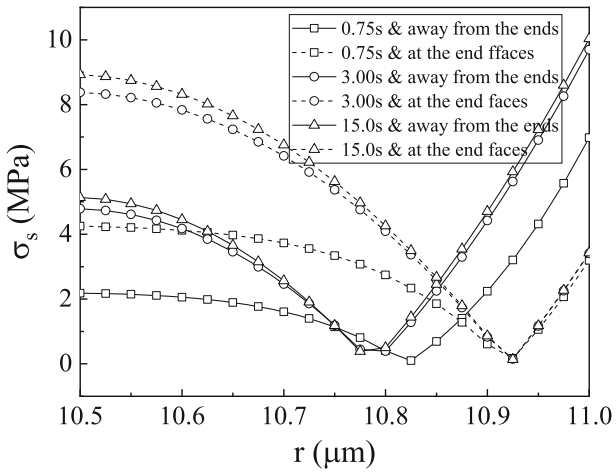

Fig. 8 The comparison of equivalent stress at end faces and away from ends under galvanostatic charging and traction free ends condition

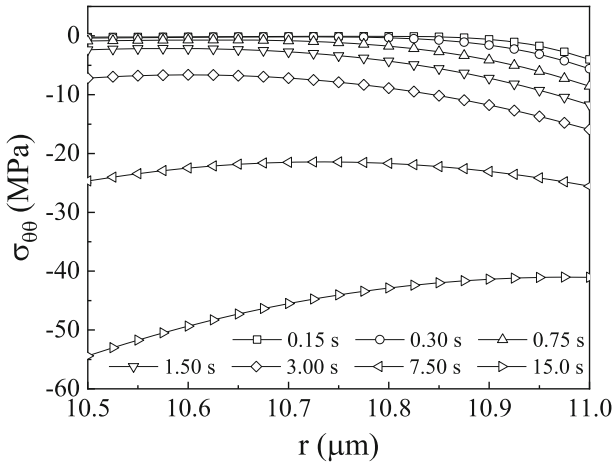

Fig. 9 Hoop stress distributions at the end faces for different times under galvanostatic charging and fixed ends condition

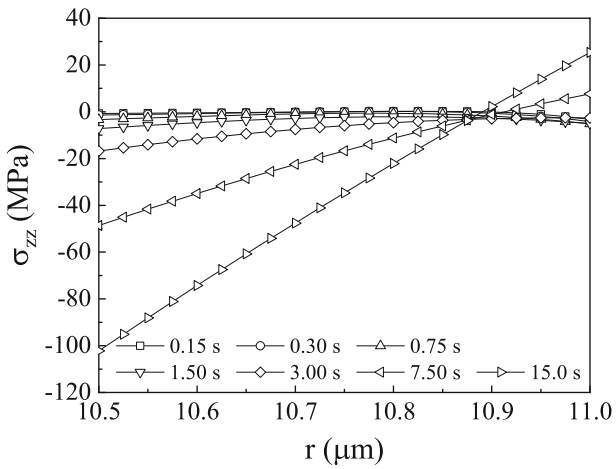

Fig. 10 Axial stress distributions at the end faces for different times under galvanostatic charging and fixed ends condition

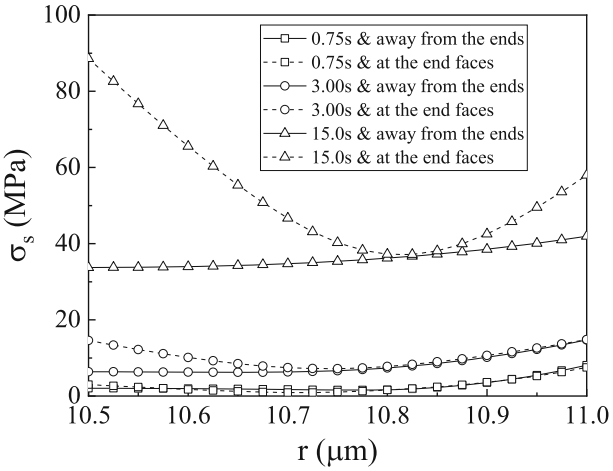

Fig. 11 The comparison of equivalent stress at end faces and away from ends under galvanostatic charging and fixed ends condition

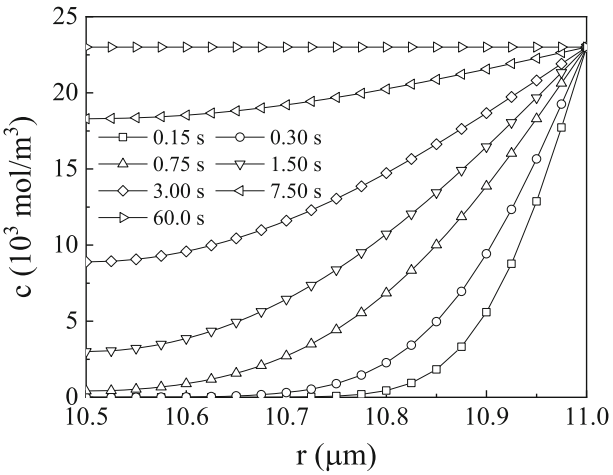

Fig. 12 The distribution of concentration at different times under potentiostatic charging

from the ends, it indicates that the fixed end produces a bending moment on the thin wall of the electrode from outside to inside, which leads to the compression on the inner edge and stretch on the outer edge.

The comparison of equivalent stress at the end faces and that away from the ends of the hollow cylindrical electrode under galvanostatic charging and fixed ends condition is shown in Fig. 11. It shows that the Mises equivalent stresses both at the end faces and away from the ends increase during the charging process, because the axial stress away from the ends, the hoop stress and axial stress at the end faces increase with the diffusion process when the ends of electrode are fixed. The maximum equivalent stress for the electrode under galvanostatic charging and fixed ends condition occurs at the inner edge of the end faces, and its value grows with the galvanostatic charging process.

4.2 The stress distribution under potentiostatic charging

The radial distribution of concentration at different times for potentiostatic operation is shown in Fig. 12. It shows that, for potentiostatic operation, the concentration at outer surface of the electrode keeps a constant value, while in the electrode the Li concentration increases with time and eventually reaches the equilibrium state where the Li concentration is uniformly distributed along the radius. The diffusion of Li concentration proceeds from the outer surfaces to the inner surface, and the diffusion rate of the concentration gradually slows down for the concentration gradient decreasing.

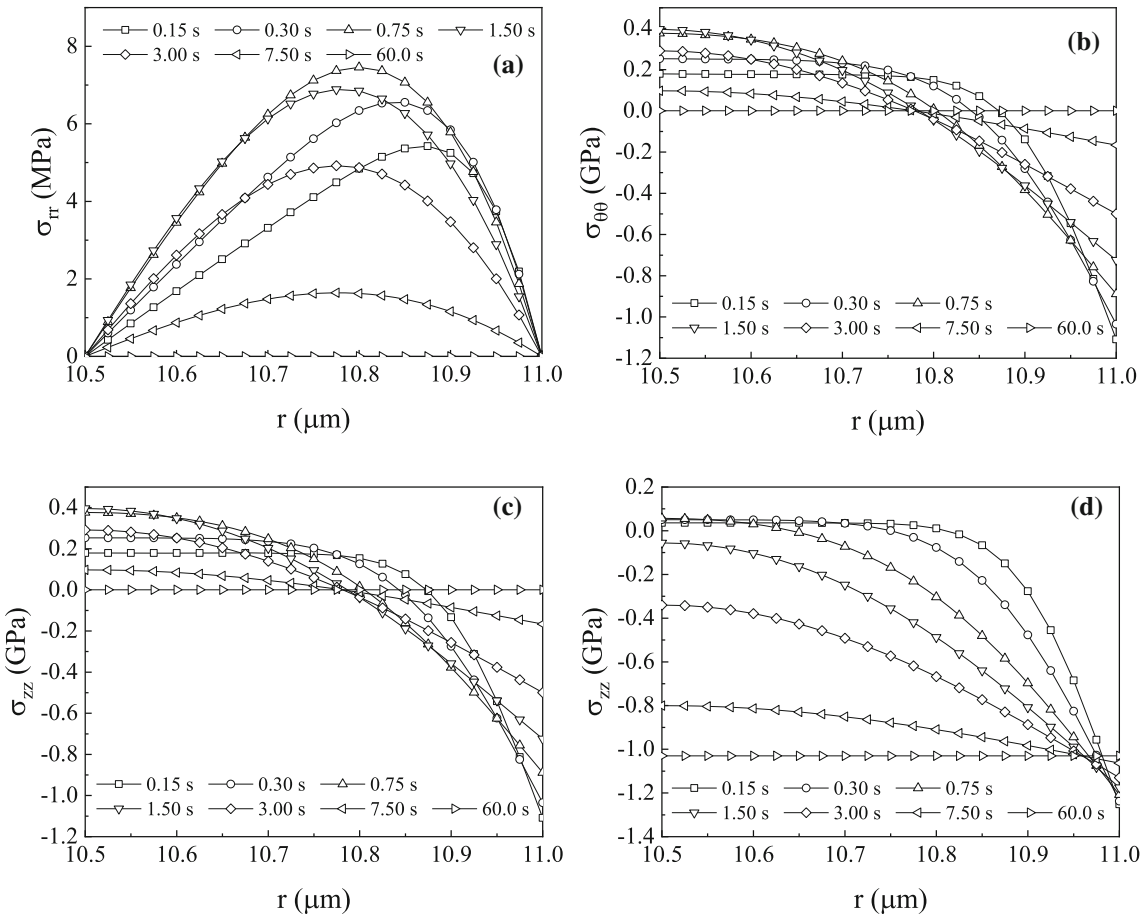

Fig. 13 Stress distributions away from the ends at different times under potentiostatic charging: **a** radial stress, **b** hoop stress, **c** axial stress under traction free ends condition, **d** axial stress under fixed ends condition

The distribution of the stresses away from the end at different times for potentiostatic operation is shown in Fig. 13. The radial stress and hoop stress independent of end conditions are shown in Figs. 13a, b, respectively. The axial stress distribution for free ends and fixed ends is shown in Figs. 13c, d, respectively. From these figures, we find that the distribution of stress remote from the ends are similar to that for galvanostatic charging; however, its value and evolution pattern are different from that for galvanostatic charging. Figure 13a shows that the radial tensile stress increases first and then decreases after about 0.75 s. The hoop stress shown in Fig. 13b presents the same trend at the inner surface, while at the outer surface, the compressive stress gradually decreases. Eventually, the radial stress and hoop stress disappear in the equilibrium state where the Li concentration is uniformly distributed. The evolution of axial stress remote from the ends under free ends condition shown in Fig. 13c is also similar to that of the hoop stress, and the reason is the same as that for galvanostatic charging. Under fixed ends condition, the axial stress away from the ends is compressive in the electrode as shown in Fig. 13d. The compressive stress increases at the inner surfaces but decreases at the outer surfaces with the diffusion processes and finally comes to the same value in the equilibrium state.

The distribution of resultant hoop stress at the end faces of the electrode with traction free ends under potentiostatic charging is shown in Fig. 14. Its evolution is identical to that of the hoop stress remote from the ends and also eliminated at last for the bending moment M disappearing when Li concentration is uniformly distributed in electrode. To analyze the end effect, the comparison of distribution of them at 0.15 s, 0.75 s and 3.00 s is also shown in Fig. 15. The tensile hoop stress at the inner edge of the end faces is increased and the value of the compressive hoop stress at the outer edge is diminished compared to the hoop stress remote from the ends at the same time. This indicates the bending moment-induced hoop tensile stress at the end faces, and the value of the induced stress is also increased first and then diminished to zero. The maximum tensile stress

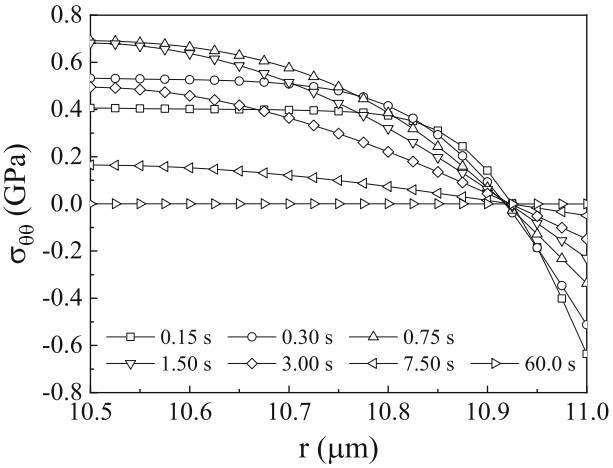

Fig. 14 Hoop stress distributions at the end faces for different times under potentiostatic charging and traction free ends condition

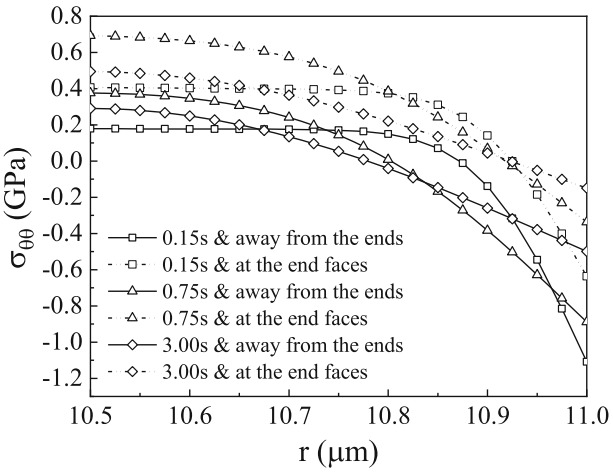

Fig. 15 The comparison of hoop stress at end faces and away from ends under potentiostatic charging and traction free ends condition

at the free end of the thin wall electrode is about 76% greater than the maximum stress at points remote from the ends under potentiostatic operation.

The von Mises equivalent stresses at end faces and away from the ends for the hollow cylindrical electrode under potentiostatic charging and traction free end condition are shown in Fig. 16. The equivalent stresses at the inner surface away from the ends and at the inner edge of end faces first increase and then decrease, while at the outer surface and outer edge, the equivalent stress gradually decreases. The maximum equivalent stress occurs at the beginning of the potentiostatic charging process, and its position is at the outer surface away from the ends of the hollow cylindrical electrode.

For the electrode with fixed ends under potentiostatic charging, the distribution of resultant hoop stress at the end faces is shown in Fig. 17. It shows that the hoop stress gets into compressive at the end faces, and its value increases at the inner edge, decreases at the outer edge and remains unchanged after reaching the equilibrium state, when the Li concentration in the electrode is uniformly distributed and no longer grows under potentiostatic charging. The maximum compressive stress at the end faces is 33% greater than the maximum compressive stress remote from the ends.

The axial stress at the end faces of the electrode with fixed ends under potentiostatic charging is shown in Fig. 18. It shows that the distribution of axial stress at the end faces under potentiostatic charging is the same as that under galvanostatic charging. However, the axial stress at the end faces under potentiostatic charging will come to a stable state when the Li concentration is uniformly distributed in the electrode at equilibrium sate.

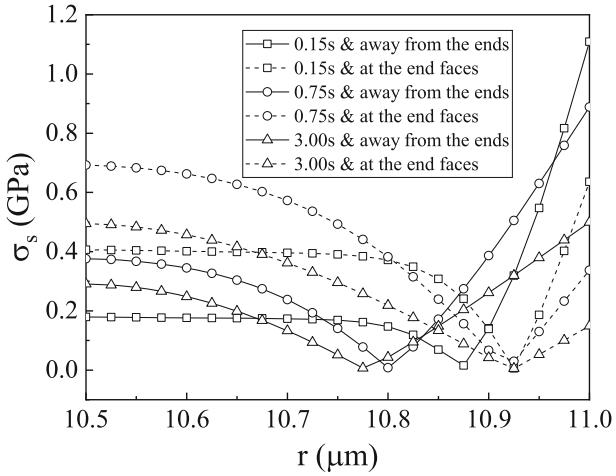

Fig. 16 The comparison of equivalent stress at end faces and away from ends under potentiostatic charging and traction free ends condition

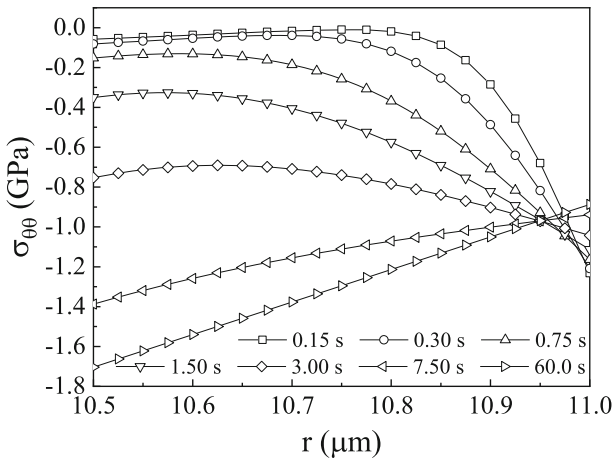

Fig.17 Hoop stress distributions at the end faces for different times under potentiostatic charging and fixed ends condition

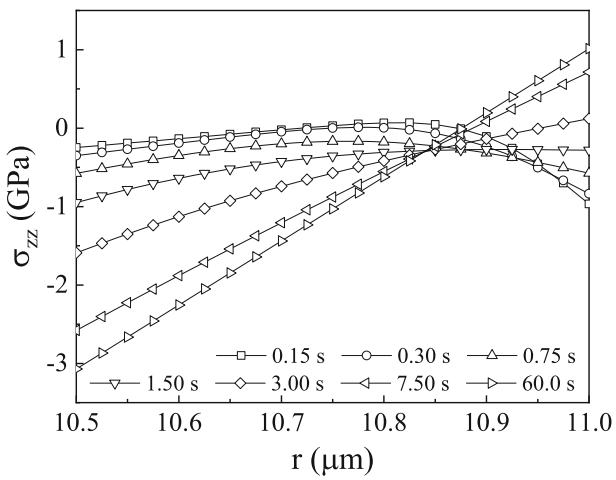

Fig. 18 Axial stress distributions at the end faces for different times under potentiostatic charging and fixed ends condition

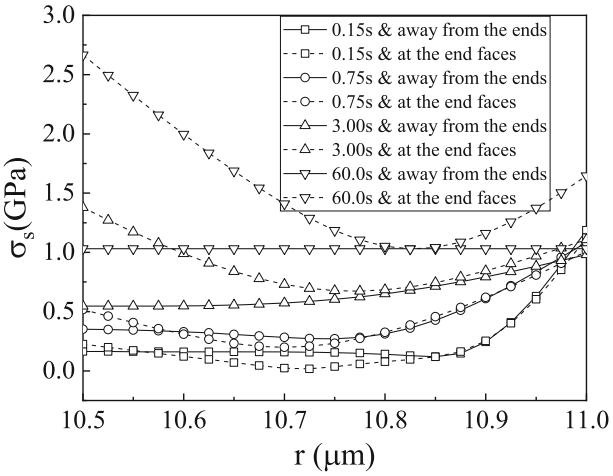

Fig. 19 The comparison of equivalent stress at end faces and away from ends under potentiostatic charging and fixed ends condition

Figure 19 shows the equivalent stress at the end faces and that away from the ends of the hollow cylindrical electrode under potentiostatic charging and fixed ends condition. The von Mises equivalent stresses at the inner surface face away from the ends and at the inner edge of end faces increase during the charging process, and the distribution of the equivalent stress in the electrode will come to a steady state for the Li concentration in the electrode uniformly distributed for the potentiostatic charging. For the electrode with both ends constrained, the maximum equivalent stress occurs at the end of the potentiostatic charging process and its position is at the inner edge of the end faces.

5 Conclusions

In this work, based on a diffusion and mechanical coupled continuum model, the diffusion-induced stresses of a thin wall hollow cylindrical electrode under either galvanostatic operation or potentiostatic operation were analytically solved. Taking into account the end effect of diffusion-induced bending near the end faces of the electrode, the analytical solutions of the stress distributions at the end faces were also obtained. Two limiting conditions at the ends of the hollow cylindrical electrode were considered: One had traction free ends and the other had fixed ends. Using the obtained analytical formulas, numerical studies were carried out to investigate the effects of end bending of the electrode, charging mode and constraint condition on the distribution of diffusion-induced stress. The numerical results showed that both charging mode and end constraint conditions affect the distribution of the diffusion-induced stress; the hoop stress at the end faces and axial stress remote from or at the end faces increase constantly under galvanostatic charging and fixed end condition. While under potentiostatic charging, the diffusion-induced stress vanishes both at and remote from the end faces at equilibrium state under traction free ends condition, and the stress distribution under fixed ends condition would also come to a stable state finally. The comparison of the stress distribution at the end faces and remote from the ends indicated that the resulting bending stresses is of practical importance for the stress distribution at the end faces. The maximum tensile stress at the free end of the thin wall electrode is 74% greater than the stress at points remote from the ends under galvanostatic operation and traction free ends condition, and under potentiostatic charging and fixed ends condition, the maximum compressive stress at the end faces is 33% greater than the maximum compressive stress remote from the ends. For the electrode with traction free ends condition, the maximum von Mises equivalent stress during the charging process, either potentiostatic charging or galvanostatic charging, occurs at the outer surface away from the ends, while for the electrode with fixed ends, the maximum equivalent stress occurs at the inner edge of the end faces.

Acknowledgements This work was supported by the National Natural Science Foundation of China under the Grant Numbers: 11932002, 11802116, 11772012 and 11632005, which are gratefully acknowledged.

References

1. Yan, P., Zheng, J., Gu, M., Xiao, J., Zhang, J.G., Wang, C.M.: Intragranular cracking as a critical barrier for high-voltage usage of layer-structured cathode for lithium-ion batteries. Nat. Commun. **8**, 14101 (2017). https://doi.org/10.1038/ncomms14101
2. Palacin, M.R., de Guibert, A.: Why do batteries fail? Science **351**(6273), 1253292 (2016). https://doi.org/10.1126/science.1253292
3. Zhang, S., Zhao, K., Zhu, T., Li, J.: Electrochemomechanical degradation of high-capacity battery electrode materials. Prog. Mater .Sci. **89**, 479–521 (2017). https://doi.org/10.1016/j.pmatsci.2017.04.014
4. Shi, F., Song, Z., Ross, P.N., Somorjai, G.A., Ritchie, R.O., Komvopoulos, K.: Failure mechanisms of single-crystal silicon electrodes in lithium-ion batteries. Nat. Commun. (2016). https://doi.org/10.1038/ncomms11886
5. Zhang, S.: Chemomechanical modeling of lithiation-induced failure in high-volume-change electrode materials for lithium ion batteries. NPJ Comput. Mater. (2017). https://doi.org/10.1038/s41524-017-0009-z
6. Mendez, J.P., Ponga, M., Ortiz, M.: Diffusive molecular dynamics simulations of lithiation of silicon nanopillars. J. Mech. Phys. Solids **115**, 123–141 (2018). https://doi.org/10.1016/j.jmps.2018.03.008
7. Koohbor, B., Sang, L., Çapraz, Ö.Ö., Gewirth, A.A.: In situ strain measurement in solid-state Li-ion battery electrodes. J. Electrochem. Soc. **168**(1), 010516 (2021). https://doi.org/10.1149/1945-7111/abd60b
8. Prussin, S.: Generation and Distribution of dislocations by solute diffusion. J. Appl. Phys. **32**(10), 1876–1881 (1961). https://doi.org/10.1063/1.1728256
9. Lee, S., Wang, W.L., Chen, J.R.: Diffusion-induced stresses in a hollow cylinder. Mater. Sci. Eng. **285**(1–2), 186–194 (2000)
10. Cheng, Y.-T., Verbrugge, M.W.: The influence of surface mechanics on diffusion induced stresses within spherical nanoparticles. J. Appl. Phys. (2008). https://doi.org/10.1063/1.3000442
11. Deshpande, R., Cheng, Y.-T., Verbrugge, M.W.: Modeling diffusion-induced stress in nanowire electrode structures. J. Power Sour. **195**(15), 5081–5088 (2010). https://doi.org/10.1016/j.jpowsour.2010.02.021
12. Zhang, X.-Y., Chen, H.-S., Fang, D.: Effects of surface stress on lithium-ion diffusion kinetics in nanosphere electrodes of lithium-ion batteries. Int. J. Mech. Sci. (2020). https://doi.org/10.1016/j.ijmecsci.2019.105323
13. Cheng, Y.-T., Verbrugge, M.W.: Evolution of stress within a spherical insertion electrode particle under potentiostatic and galvanostatic operation. J. Power Sour. **190**(2), 453–460 (2009). https://doi.org/10.1016/j.jpowsour.2009.01.021
14. Yang, X.-G., Bauer, C., Wang, C.-Y.: Sinusoidal current and stress evolutions in lithium-ion batteries. J. Power Sour. **327**, 414–422 (2016). https://doi.org/10.1016/j.jpowsour.2016.07.070
15. Deshpande, R., Qi, Y., Cheng, Y.-T.: Effects of concentration-dependent elastic modulus on diffusion-induced stresses for battery applications. J. Electrochem. Soc. **157**(8), A967–A971 (2010). https://doi.org/10.1149/1.3454762
16. Cai, X., Guo, Z.: Influence of Li concentration-dependent diffusion coefficient and modulus hardening on diffusion-induced stresses in anisotropic anode particles. J. Electrochem. Soc. **168**(1), 010517 (2021). https://doi.org/10.1149/1945-7111/abd82e
17. Deshpande, R., Cheng, Y.-T., Verbrugge, M.W., Timmons, A.: Diffusion induced stresses and strain energy in a phase-transforming spherical electrode particle. J. Electrochem. Soc. **158**(6), A718–A724 (2011). https://doi.org/10.1149/1.3565183
18. Zhang, X., Hao, F., Chen, H., Fang, D.: Diffusion-induced stress and delamination of layered electrode plates with composition-gradient. Mech. Mater. **91**, 351–362 (2015)
19. Hu, H., Yu, P., Suo, Y.: Stress induced by diffusion and local chemical reaction in spherical composition-gradient electrodes. Acta Mech. **231**(7), 2669–2678 (2020). https://doi.org/10.1007/s00707-020-02652-4
20. Christensen, J., Newman, J.: Stress generation and fracture in lithium insertion materials. J. Solid State Electrochem. **10**(5), 293–319 (2006). https://doi.org/10.1007/s10008-006-0095-1
21. Bower, A.F., Guduru, P.R., Sethuraman, V.A.: A finite strain model of stress, diffusion, plastic flow, and electrochemical reactions in a lithium-ion half-cell. J. Mech. Phys. Solids **59**(4), 804–828 (2011). https://doi.org/10.1016/j.jmps.2011.01.003
22. Zhang, X., Shyy, W., Sastry, A.M.: Numerical simulation of intercalation-induced stress in Li-ion battery electrode particles. J. Electrochem. Soc. **154**(10), A910–A916 (2007). https://doi.org/10.1149/1.2759840
23. Bower, A.F., Guduru, P.R., Chason, E.: Analytical solutions for composition and stress in spherical elastic-plastic lithium-ion electrode particles containing a propagating phase boundary. Int. J. Solids Struct. **69–70**, 328–342 (2015). https://doi.org/10.1016/j.ijsolstr.2015.05.018
24. Christensen, J., Newman, J.: A mathematical model of stress generation and fracture in lithium manganese oxide. J. Electrochem. Soc. **153**(6), A1019–A1030 (2006). https://doi.org/10.1149/1.2185287
25. Cui, Z., Gao, F., Qu, J.: A finite deformation stress-dependent chemical potential and its applications to lithium ion batteries. J. Mech. Phys. Solids **60**(7), 1280–1295 (2012). https://doi.org/10.1016/j.jmps.2012.03.008
26. Anand, L.: A Cahn-Hilliard-type theory for species diffusion coupled with large elastic-plastic deformations. J. Mech. Phys. Solids **60**(12), 1983–2002 (2012). https://doi.org/10.1016/j.jmps.2012.08.001
27. Zhang, K., Li, Y., Wang, F., Zheng, B., Yang, F., Lu, D.: An analytical model for lithiation-induced concurrent plastic flow and phase transformation in a cylindrical silicon electrode. Int. J. Solids Struct. **202**, 87–98 (2020). https://doi.org/10.1016/j.ijsolstr.2020.06.008
28. Chen, Y., Chen, H., Luan, W.: Shakedown, ratcheting and fatigue analysis of cathode coating in lithium-ion battery under steady charging-discharging process. J. Mech. Phys. Solids **150**, 104366 (2021). https://doi.org/10.1016/j.jmps.2021.104366
29. Drozdov, A.D.: A model for the mechanical response of electrode particles induced by lithium diffusion in Li-ion batteries. Acta Mech. **225**(11), 2987–3005 (2014). https://doi.org/10.1007/s00707-014-1096-2
30. Bagheri, A., Arghavani, J., Naghdabadi, R., Brassart, L.: A theory for coupled lithium insertion and viscoplastic flow in amorphous anode materials for Li-ion batteries. Mech. Mater. (2021). https://doi.org/10.1016/j.mechmat.2020.103663

31. Larché, F., Cahn, J.W.: A linear theory of thermochemical equilibrium of solids under stress. Acta Metall. **21**(8), 1051–1063 (1973). https://doi.org/10.1016/0001-6160(73)90021-7
32. Liu, Y., Lv, P., Ma, J., Bai, R., Duan, H.L.: Stress fields in hollow core-shell spherical electrodes of lithium ion batteries. Proc. R. Soc. A Math. Phys. Eng. Sci. (2014). https://doi.org/10.1098/rspa.2014.0299
33. Haftbaradaran, H., Qu, J.: Two-dimensional chemo-elasticity under chemical equilibrium. Int. J. Solids Struct. **56–57**, 126–135 (2015). https://doi.org/10.1016/j.ijsolstr.2014.11.025
34. Gao, X., Fang, D., Qu, J.: A chemo-mechanics framework for elastic solids with surface stress. Proc. R. Soc. A Math. Phys. Eng. Sci. (2015). https://doi.org/10.1098/rspa.2015.0366
35. Ryu, I., Choi, J.W., Cui, Y., Nix, W.D.: Size-dependent fracture of Si nanowire battery anodes. J. Mech. Phys. Solids **59**(9), 1717–1730 (2011). https://doi.org/10.1016/j.jmps.2011.06.003
36. Eshghinejad, A., Li, J.: The coupled lithium ion diffusion and stress in battery electrodes. Mech. Mater. **91**, 343–350 (2015). https://doi.org/10.1016/j.mechmat.2015.09.015
37. Bagheri, A., Arghavani, J., Naghdabadi, R.: On the effects of hydrostatic stress on Li diffusion kinetics and stresses in spherical active particles of Li-ion battery electrodes. Mech. Mater. (2019). https://doi.org/10.1016/j.mechmat.2019.103134
38. Chen, H., Huang, H.-Y.S.: Modeling and simulation of the non-equilibrium process for a continuous solid solution system in lithium-ion batteries. Int. J. Solids Struct. **212**, 124–142 (2021). https://doi.org/10.1016/j.ijsolstr.2020.11.014
39. Holzapfel, M., Buqa, H., Scheifele, W., Novak, P., Petrat, F.M.: A new type of nano-sized silicon/carbon composite electrode for reversible lithium insertion. Chem. Commun. **12**, 1566–1568 (2005). https://doi.org/10.1039/b417492e
40. Patel, P., Kim, I.S., Kumta, P.N.: Nanocomposites of silicon/titanium carbide synthesized using high-energy mechanical milling for use as anodes in lithium-ion batteries. Mater. Sci. Eng. B Solid State Mater. Adv. Technol. **116**(3), 347–352 (2005). https://doi.org/10.1016/j.mseb.2004.05.046
41. Zhu, X., Xie, Y., Chen, H., Luan, W.: Numerical analysis of the cyclic mechanical damage of Li-ion battery electrode and experimental validation. Int. J. Fatigue **142**, 105915 (2021). https://doi.org/10.1016/j.ijfatigue.2020.105915
42. Chan, C.K., Peng, H., Liu, G., McIlwrath, K., Zhang, X.F., Huggins, R.A., Cui, Y.: High-performance lithium battery anodes using silicon nanowires. Nat. Nanotechnol. **3**(1), 31–35 (2008). https://doi.org/10.1038/nnano.2007.411
43. Xiao, X., Liu, P., Verbrugge, M.W., Haftbaradaran, H., Gao, H.: Improved cycling stability of silicon thin film electrodes through patterning for high energy density lithium batteries. J. Power Sour. **196**(3), 1409–1416 (2011). https://doi.org/10.1016/j.jpowsour.2010.08.058
44. Bhandakkar, T.K., Gao, H.: Cohesive modeling of crack nucleation in a cylindrical electrode under axisymmetric diffusion induced stresses. Int. J. Solids Struct. **48**(16–17), 2304–2309 (2011). https://doi.org/10.1016/j.ijsolstr.2011.04.005
45. Yao, Y., McDowell, M.T., Ryu, I., Wu, H., Liu, N., Hu, L., Nix, W.D., Cui, Y.: Interconnected silicon hollow nanospheres for lithium-ion battery anodes with long cycle life. Nano Lett. **11**(7), 2949–2954 (2011). https://doi.org/10.1021/nl201470j
46. Zhang, K., Li, Y., Zheng, B., Wu, G., Wu, J., Yang, F.: Large deformation analysis of diffusion-induced buckling of nanowires in lithium-ion batteries. Int. J. Solids Struct. **108**, 230–243 (2017). https://doi.org/10.1016/j.ijsolstr.2016.12.020
47. Zhang, K., Li, Y., Wu, J., Zheng, B., Yang, F.: Lithiation-induced buckling of wire-based electrodes in lithium-ion batteries: a phase-field model coupled with large deformation. Int. J. Solids Struct. **144–145**, 289–300 (2018). https://doi.org/10.1016/j.ijsolstr.2018.05.014
48. Zhang, K., Li, Y., Wang, F., Zheng, B., Yang, F.: Stress effect on self-limiting lithiation in silicon-nanowire electrode. Appl. Phys. Express (2019). https://doi.org/10.7567/1882-0786/ab0ce8
49. Xing, H., Liu, Y., Wang, B.: Mechano-electrochemical and buckling analysis of composition-gradient nanowires electrodes in lithium-ion battery. Acta Mech. **230**(12), 4145–4156 (2019). https://doi.org/10.1007/s00707-019-02486-9
50. Zhang, Y., Zhan, S., Zhang, K., Zheng, B., Lyu, L.: Buckling behavior of a wire-like electrode with a concentration-dependent elastic modulus based on a deformed configuration. Eur. J. Mech. A. Solids **85**, 104111 (2021). https://doi.org/10.1016/j.euromechsol.2020.104111
51. Chakraborty, J., Please, C.P., Goriely, A., Chapman, S.J.: Combining mechanical and chemical effects in the deformation and failure of a cylindrical electrode particle in a Li-ion battery. Int. J. Solids Struct. **54**, 66–81 (2015). https://doi.org/10.1016/j.ijsolstr.2014.11.006
52. Guo, Z., Zhang, T., Hu, H., Song, Y., Zhang, J.: Effects of hydrostatic stress and concentration-dependent elastic modulus on diffusion-induced stresses in cylindrical li-ion batteries. J. Appl. Mech. (2013). https://doi.org/10.1115/1.4025271
53. Yang, F.: Effect of diffusion-induced bending on diffusion-induced stress near the end faces of an elastic hollow cylinder. Mech. Res. Commun. **51**, 72–77 (2013). https://doi.org/10.1016/j.mechrescom.2013.05.006
54. Zhang, X.L., Zhong, Z.: A coupled theory for chemically active and deformable solids with mass diffusion and heat conduction. J. Mech. Phys. Solids **107**, 49–75 (2017). https://doi.org/10.1016/j.jmps.2017.06.013
55. Wang, X.-Q., Yang, Q.-S.: An analytical solution for chemo-mechanical coupled problem in deformable sphere with mass diffusion. Int. J. Appl. Mech. (2020). https://doi.org/10.1142/s1758825120500763
56. Haftbaradaran, H., Song, J., Curtin, W.A., Gao, H.: Continuum and atomistic models of strongly coupled diffusion, stress, and solute concentration. J. Power Sour. **196**(1), 361–370 (2011). https://doi.org/10.1016/j.jpowsour.2010.06.080
57. Timoshenko, S.: Strength of Materials, Part 2: Advanced Theory and Problems, 3rd edn. Van Nostrand Reinhold Company, New York (1958)
58. Crank, J.: The Mathematics of Diffusion, 2nd edn. Oxford University Press, Oxford (1975)
59. Song, Y., Lu, B., Ji, X., Zhang, J.: Diffusion induced stresses in cylindrical lithium-ion batteries: analytical solutions and design insights. J. Electrochem. Soc. **159**(12), A2060–A2068 (2012). https://doi.org/10.1149/2.079212jes
60. Song, X., Lu, Y., Wang, F., Zhao, X., Chen, H.: A coupled electro-chemo-mechanical model for all-solid-state thin film Li-ion batteries: The effects of bending on battery performances. J. Power Sour. (2020). https://doi.org/10.1016/j.jpowsour.2020.227803